



#### OPEN ACCESS

EDITED BY  
Samiran Mandal,  
Indian Institute of Technology Delhi, India

REVIEWED BY  
Tien Anh Tran,  
Seoul National University,  
Republic of Korea  
Efrain Moreles,  
National Autonomous University of  
Mexico, Mexico

\*CORRESPONDENCE  
Daniel G. MacDonald  
✉ dmacdonald@umassd.edu

<sup>†</sup>Deceased

RECEIVED 01 December 2025  
REVISED 19 February 2026  
ACCEPTED 20 February 2026  
PUBLISHED 25 March 2026

#### CITATION

MacDonald DG and Goodman L (2026)  
Defining an appropriate range of  
scales for application of the gradient  
Richardson number, with implications  
for observations of stratified shear  
turbulence at laboratory  
and ocean scales.  
*Front. Mar. Sci.* 13:1758561.  
doi: 10.3389/fmars.2026.1758561

#### COPYRIGHT

© 2026 MacDonald and Goodman. This is  
an open-access article distributed under  
the terms of the [Creative Commons  
Attribution License \(CC BY\)](https://creativecommons.org/licenses/by/4.0/). The use,  
distribution or reproduction in other  
forums is permitted, provided the  
original author(s) and the copyright  
owner(s) are credited and that the  
original publication in this journal is  
cited, in accordance with accepted  
academic practice. No use, distribution  
or reproduction is permitted which does  
not comply with these terms.

# Defining an appropriate range of scales for application of the gradient Richardson number, with implications for observations of stratified shear turbulence at laboratory and ocean scales

Daniel G. MacDonald<sup>1,2\*</sup> and Louis Goodman<sup>2†</sup>

<sup>1</sup>Department of Civil and Environmental Engineering, University of Massachusetts Dartmouth, North Dartmouth, MA, United States, <sup>2</sup>Department of Estuarine and Ocean Science, University of Massachusetts Dartmouth, North Dartmouth, MA, United States

The Richardson number ( $Ri$ ) represents the square of the ratio of buoyancy frequency to vertical shear, and a value less than  $\frac{1}{4}$  has long been recognized as a necessary condition for the generation of turbulence, particularly at small scales. At larger scales, it is common to evaluate a bulk Richardson number, ( $Ri_B$ ), with arbitrary values of criticality, generally greater than  $\frac{1}{4}$ . Despite the ubiquity of this concept in modern oceanography, the range of scales over which the critical value of  $\frac{1}{4}$  is valid has not been well documented. Here, spectral and energetics arguments are used to identify the primitive shear length scale,  $l_s = (\frac{\nu}{S})^{\frac{1}{2}}$ , where  $\nu$  is kinematic viscosity and  $S$  is velocity shear, as the fundamental scale for appropriate scales for a critical value of  $Ri = \frac{1}{4}$ . These findings are evaluated against a variety of data, suggesting that the range  $10 l_s - 100 l_s$  is an approximate range of validity for the critical value of  $\frac{1}{4}$ . This range is equivalent to  $100 < Re < 10,000$ , where  $Re$  is a Reynolds number based on thickness and velocity across the layer. Further data analysis suggests that turbulence persists at values of  $Ri_B$  far above  $\frac{1}{4}$  in very thick layers ( $Re > 10^5$ ), and that turbulence intensity is enhanced for thin layers ( $Re < 10^5$ ). We hypothesize the former is due to the existence of smaller scale regions within the layer where  $Ri$  locally falls below  $\frac{1}{4}$ , while the latter is the result of stratification increasing the ratio of turbulent kinetic energy to fluid mass. Historically, the value of  $Re$  has been considered of minimal relevance to stratified turbulence in the ocean. However, here we demonstrate the significance of  $Re$ , and suggest a broader view of turbulence within  $Re$ - $Ri$  parameter space. The proposed parameter space may potentially yield new insights into turbulence closures, particularly at lower  $Re$  values, provide a more rigorous approach to defining critical values of  $Ri_B$ , greatly facilitating interpretation of observational data, and provide a more rigorous framework for the use of direct numerical simulation (DNS) results and laboratory experiments of turbulence to inform geophysical scale dynamics.

#### KEYWORDS

criticality, mixing, Reynolds number, Richardson number, stratified shear turbulence

# 1 Introduction

Turbulence in stratified shear environments is a key aspect of many oceanographic flows, from deep ocean overflows, such as the Mediterranean outflow (e.g., [Baringer and Price, 1997](#)) or Faroes Bank overflow ([Fer et al., 2010](#)), which are characterized by stratified-shear layers 100s of meters or more in thickness, to estuarine and river plume systems (e.g., [MacDonald et al., 2007](#); [Kilcher et al., 2012](#)), with layer thicknesses on the order of meters, and even salt marsh – tidal flat exchanges (e.g. [Carr et al., 2018](#)), with layers on the order of 10s of cm. Given the importance and relative complexity of these flows, researchers have long turned to laboratory experiments (e.g., [Ellison and Turner, 1959](#); [Yuan and Horner-Devine, 2013](#)), and more recently Direct Numerical Simulations (DNS) (e.g. [Shih et al., 2000](#); [Smyth et al., 2001](#); [Mashayek et al., 2017](#)), for insight into their dynamics.

Turbulence in unbounded stratified-shear environments is characterized by the presence of gradients in both density and velocity, generating competing influences towards stability and instability, respectively, and typically characterized by a Richardson number, which can be written in general form as:

$$Ri = N^2 S^{-2} \quad (1)$$

where  $N = \left(-\frac{g}{\rho_0} \frac{\partial \rho}{\partial z}\right)^{\frac{1}{2}}$  is a buoyancy frequency, and  $S = \frac{\partial u}{\partial z}$  represents the vertical shear of horizontal velocity. Here,  $g$  is gravitational acceleration,  $\rho$  is density (with  $\rho_0$  a representative value) and  $u$  the horizontal velocity component. Depending on the vertical resolution associated with both  $N$  and  $S$ , there are various interpretations of the Richardson number. At sufficiently small scales, as noted by [Miles \(1961\)](#) and [Howard \(1961\)](#), the Richardson number is commonly referred to as a gradient Richardson number,  $Ri_g$ , for which a value less than or equal to 0.25 is a necessary condition for the generation of instabilities and turbulence. At larger scales, the Richardson number is often referred to as a Bulk Richardson number,  $Ri_B$ . Traditionally, a critical value for  $Ri_B$  higher than  $\frac{1}{4}$  (typically on the order of 0.5 – 1, or higher) is considered based on observations, but there is no consensus on an appropriate value and little analytical/theoretical underpinning for its assessment (e.g., [Fong and Geyer, 2001](#); [Pollard et al., 1973](#); [Price et al., 1986](#); [Nathaniel et al., 2024](#)).

Turbulence in stratified shear environments can be initiated by the development of vortices, such as Kelvin-Helmholtz (K-H) billows ([Thorpe, 1969](#)), or Holmboe instabilities (e.g., [Smyth and Peltier, 1989](#); [Lawrence et al., 2013](#); [Salehipour et al., 2016a](#)), which

subsequently decay to turbulence, as shown in [Figure 1](#). Here, the fluids at the top and bottom are of constant velocity and density, and are separated by a stratified-shear layer, of order  $h$  in vertical extent. The entire flow structure is distant from any boundaries.

The outer, or overturning, scale of the K-H process (e.g., [Figure 1](#)) is related to the Ozmidov scale (e.g. [Gregg, 1987](#)),  $L_O = (\varepsilon N^{-3})^{\frac{1}{2}}$ , where  $\varepsilon$  represents the rate of dissipation of turbulent kinetic energy (TKE). The ratio of the overturning scale to the Ozmidov scale is a function of the turbulence age (e.g. [Smyth et al., 2001](#)), and is typically of order one ([Ferron et al., 1998](#); [MacDonald et al., 2013](#)) for a fully developed K-H billow, with the ratio of turbulent to Ozmidov scales decreasing as the turbulence ages ([Wijesekera and Dillon, 1997](#); [Smyth and Moum, 2000](#)). However, the initiation of instabilities can be triggered at scales much smaller than the Ozmidov scale, presumably within isolated regions where the local value of  $Ri_g$  falls below  $\frac{1}{4}$ . As turbulence evolves, energy initially contained within the larger scale overturns cascades to smaller and smaller eddy sizes until the transfer of energy is constrained by the conversion of TKE to heat by the fluid viscosity. These dissipative scales are characterized by the Kolmogorov scale,  $\eta = (\nu^3 \varepsilon^{-1})^{\frac{1}{4}}$ , where  $\nu$  is the kinematic viscosity. Similar dissipative processes for scalars (e.g., heat and/or salinity) occur at the analogous Batchelor scales. For ocean turbulence,  $L_O \gg \eta$ , and both scales may be fundamentally different than the shear layer thickness,  $h$ , as illustrated in [Figure 1](#).

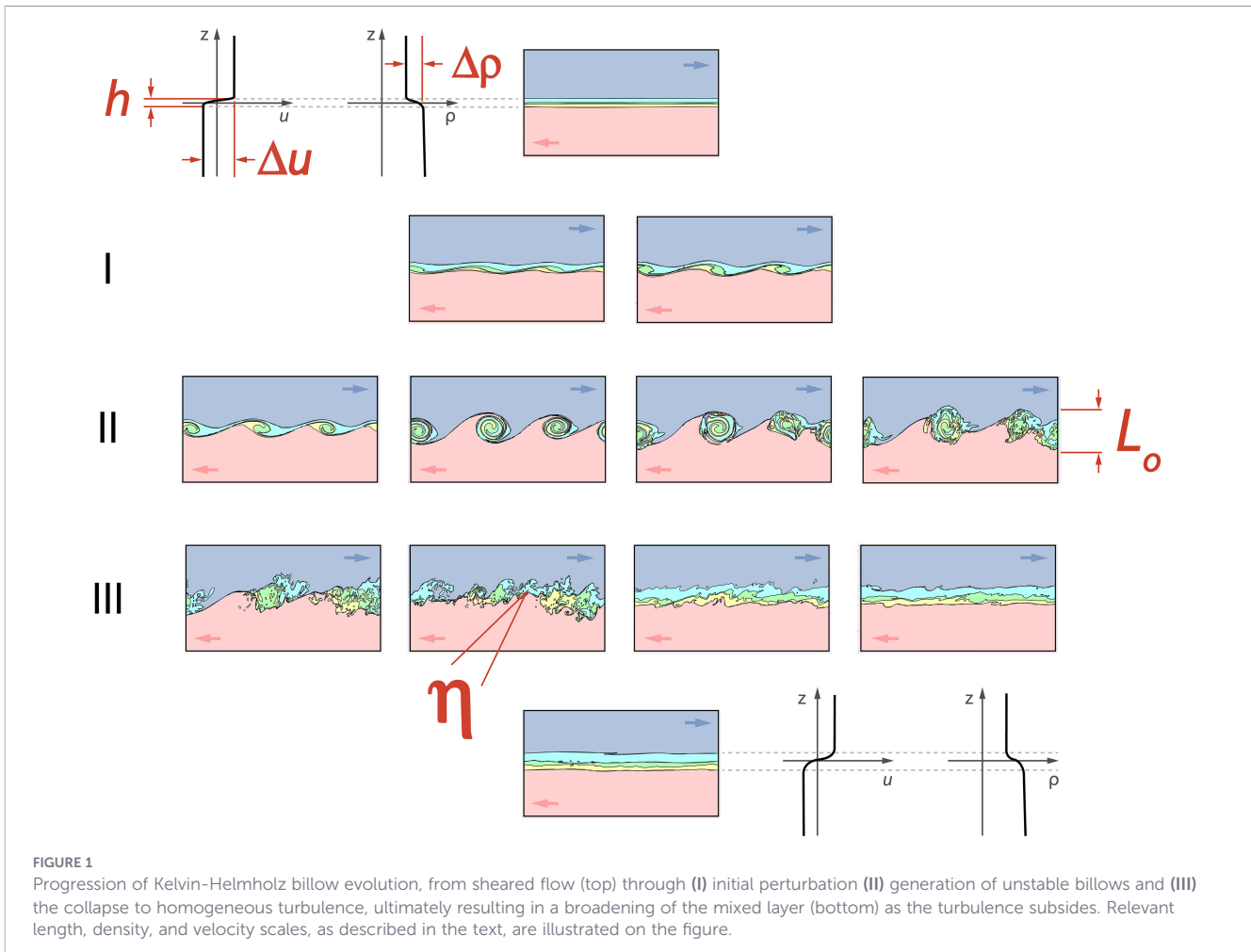
Because of difficulties in measuring the gradients in (1) precisely at sufficiently small scales,  $Ri_B$  is often used in analyzing observational data and ocean model output. Taken across a shear stratified region with a vertical extent of  $h$  (analogous to [Figure 1](#)),  $Ri_B$  can also be written as:

$$Ri_B = g' h (\Delta u)^{-2} \quad (2)$$

where the reduced gravity,  $g' = g \frac{\Delta \rho}{\rho_0}$ , and the velocity difference,  $\Delta u$ , are representative of changes across the vertical distance  $h$ .

[Figure 2](#) shows profiles of density and velocity from the highly energetic and stratified Merrimack River plume environment ([Piffer Braga et al., 2025](#)), along with a corresponding Richardson number profile. Note that, as is common in many observational scenarios, a mismatch exists between vertical resolution of density ( $\sim 1$  cm) and velocity ( $\sim 25$  cm), and thus the resolution of the calculated Richardson number is driven largely by the least resolved variable (velocity in this case), with variability driven by the more resolved variable (e.g. density). Note also that local (i.e., more highly resolved) values of the Richardson number throughout the layer can be distinctly different from the mean value of  $Ri_B$  across the layer (shown by the dotted vertical line), due to inherent variability in the gradients at smaller scales. In this case, the mean value is greater than  $\frac{1}{4}$ , although much of the region falls below  $\frac{1}{4}$  (at the resolved scales). Whether either variable in this case is resolved to an appropriate level such that the calculated Richardson number can be truly considered a gradient  $Ri_g$  is unknown. Alternatively, all the values could, in essence, be considered bulk values. In practice, when considering observational or model-derived data, either a bulk Richardson number is considered, with reference to an essentially arbitrary critical value, or the most highly resolved estimate available is considered a *de facto* gradient Richardson

**Abbreviations:** Ri, A generic representation of the Richardson number,  $Ri = N^2 S^{-2}$ ;  $Ri_g$ , A Richardson number evaluated over scales small enough to satisfy the critical condition of  $\frac{1}{4}$ ;  $Ri_B$ , A Richardson number evaluated over scales larger than the gradient range (see  $Ri_g$ ); Re, A Reynolds number evaluated across the entire thickness of the stratified shear layer;  $Re_t$ , A Reynolds number evaluated across the turbulent scales;  $Re_b$ , The buoyancy Reynolds number, representing the ratio of Ozmidov to Kolmogorov scales;  $Re_s$ , A shear Reynolds number;  $C_D$ , An interfacial drag coefficient;  $Ri_f$ , The buoyancy flux, representing the ratio of buoyancy flux to production in the Turbulent Kinetic Energy Equation; E, The entrainment coefficient, representing the ratio of entrainment velocity to bulk velocity.



number value, without any confirmation of its resolution. Either approach can result in flawed interpretations of the underlying dynamics.

We have identified the importance of scale for the interpretation of the Richardson number. Similarly, the interpretation of other key diagnostic parameters of turbulence can also be affected by scale. We refer to the layer Reynolds number as:

$$Re = \Delta u h / \nu \tag{3}$$

while the turbulent Reynolds number is defined as:

$$Re_t = u_* l_* / \nu \tag{4}$$

where  $u_*$  and  $l_*$  represent velocity and length scales, respectively, associated with a turbulent eddy, which may vary in size. If  $\bar{S}$  represents the mean shear over the layer, then the root mean square (rms) turbulent velocity can be estimated as  $u_* = \frac{1}{2} \bar{S} l_*$ , such that  $Re_t = \frac{1}{2} \bar{S} l_*^2 / \nu$ . Furthermore, a buoyancy Reynolds number can be defined as:

$$Re_b = \epsilon / \nu N^2 \tag{5}$$

which is related to the ratio of the Ozmidov scale to the Kolmogorov scale (Kolmogorov, 1941), and thus represents the

dynamic extent of the inertial subrange. By analogy a shear Reynolds number can be defined as:

$$Re_S = \epsilon / \nu S^2 \tag{6}$$

Note that (Equations 5, 6) could be implemented at any vertical scale, and often implemented at larger scales in observational studies (e.g., Delatolas et al., 2023) and at turbulent scales in modeling studies (e.g. Bartello and Tobias, 2013). By convention, we will assume that both quantities are taken at the turbulent scale, unless otherwise noted. It is interesting to note that the ratio of the shear and buoyancy Reynolds numbers returns a Richardson number at an appropriate vertical scale:

$$Ri = \frac{Re_S}{Re_b} \tag{7}$$

The layer scale and turbulent scales are straightforward to interpret, particularly with the understanding that a range of turbulent scales exists between the Ozmidov scale on one end and the Kolmogorov scale on the other. However, the appropriate scales for the gradient Richardson number are not clear. On the one hand, we could ask “how small is ‘small enough’ for a  $Ri$  estimate to be considered a gradient  $Ri_g$ ?” More specifically we could focus on the following questions:

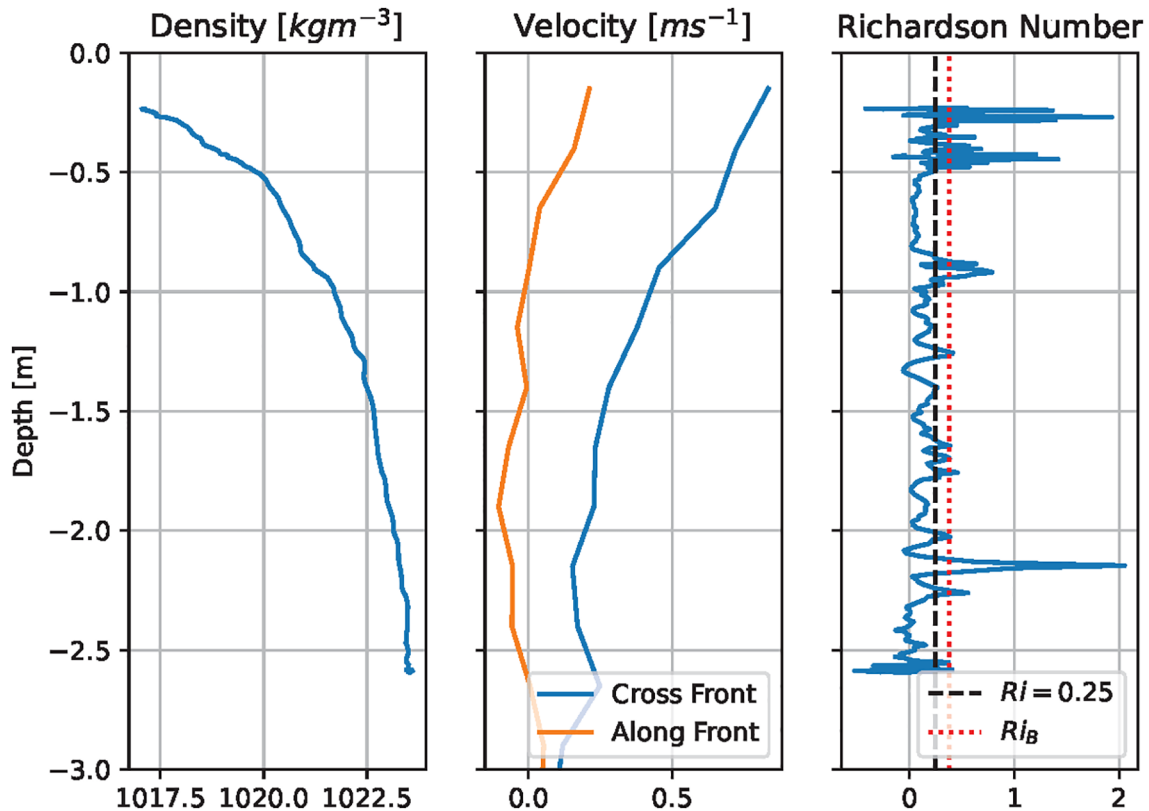


FIGURE 2

Example profiles of density, velocity and  $Ri$ , from a river plume frontal region in the coastal ocean (Merrimack River plume, see Piffer Braga et al., 2025). Note resolution mismatch between density ( $\sim 1$  cm) and velocity ( $\sim 25$  cm), thus estimates of  $Ri$  are biased by the lower resolution of the velocity measurements. The bold dashed line in the left panel indicates the critical value for  $Ri_g$  of  $1/4$ , while the red dotted line represents the average value of  $Ri$  over the entire region (i.e.,  $Ri_B$ ).

- What is the smallest scale where the critical value of  $Ri_g = 1/4$  is valid?
- At what scales does the transition from  $Ri_g$  to  $Ri_B$  occur?

These two questions serve to define the lower and upper bounds of the “gradient range”, where  $Ri = Ri_g < 1/4$  is an appropriate threshold (necessary but not sufficient) for initiation of turbulence. We refer to the lower end of this range as the “gradient scale”. The Kolmogorov scale has long been recognized as an appropriate scale for the dissipative demise of turbulence, where the energetics of small eddies can no longer overcome the frictional effects of fluid viscosity, and the associated energy is thus dissipated to heat (e.g., Tennekes and Lumley, 1972). Does a similar scale exist for the initiative stages of turbulence, representing the minimum scale required for an instability to break the bonds of fluid viscosity, resulting in an evolving disturbance that transitions into turbulence? Such a scale would define the gradient scale, illuminating not only the small scale dynamics of turbulence generation but also providing a mechanism for the generation and maintenance of turbulence at higher values of  $Ri_B$ . This in turn might lead towards a more defensible estimate of a critical value for  $Ri_B$ , and a refinement of parameterizations for stratified shear turbulence based solely on Richardson number. An understanding of the gradient scale will provide significant insight and context into the interpretation of observational oceanographic

turbulence data, and will allow for more effective comparisons between laboratory/DNS scale turbulence and geophysical scale turbulence.

Section 2 of this manuscript explores the stability of stratified shear layers using a wavenumber criteria to define regions of stability, and relating these findings to a “primitive shear length scale”, which we relate to the gradient scale. Section 3 explores the relevance of this scaling using observational and laboratory data from the literature, across a wide range of scales, constraining the gradient range. Section 4 discusses the implications of the new scaling, particularly its potential utility in connecting turbulent simulations and observations across vast scale differences. We also discuss the issue of critical  $Ri_B$  values as a function of scale.

## 2 An heuristic approach to viscous stability of a stratified shear layer

Consider a stratified shear region in the ocean similar to Figure 1, with thickness  $h$ , and approximately constant buoyancy frequency,  $N$ , and mean shear,  $\bar{S}$ . The magnitude of the horizontal velocity field within the layer is given by  $\Delta u = \bar{S}h$ , and the rms turbulent velocity by  $u_* = \frac{1}{2}\bar{S}l_*$ . For this common scenario, two regions of stability exist:

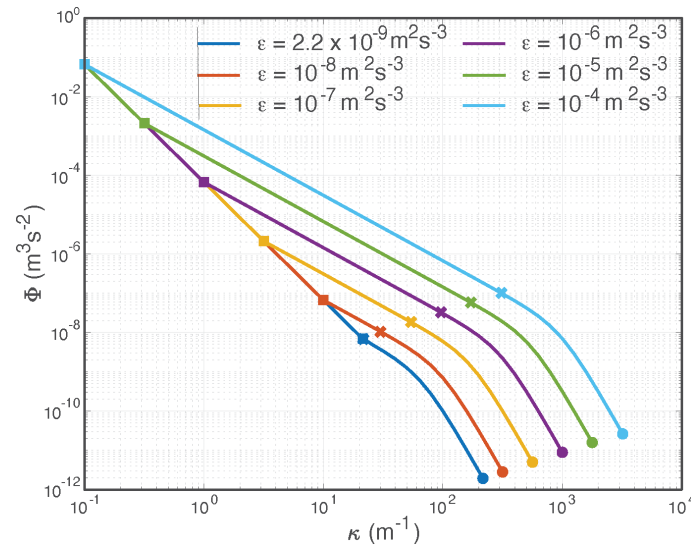


**FIGURE 3** Equations 8(a, b) plotted for  $N = 0.01 \text{ s}^{-1}$ , and a range of turbulent kinetic energy (TKE) dissipation values,  $\epsilon$ . Squares represent the Ozmidov lengthscale, and the boundary of  $Ri=1/4$ . Circles represent the Kolmogorov lengthscale, and x's represent  $\kappa_c$  with  $\gamma=10$ .  $\epsilon$  increases from left to right, as indicated by the legend at the top of the figure.

- Region I: Stable for  $Ri_g > Ri_{critical} = \frac{1}{4}$ , with buoyancy dominating shear, and
- Region II: Stable for  $Ri_g < Ri_{critical} = \frac{1}{4}$  with shear dominating buoyancy but unable to overcome viscous effects. This is consistent with the understanding that a subcritical Richardson number (i.e.,  $<1/4$ ) is a necessary, but not sufficient condition for instability.

We consider these two regions through the context of turbulent spectra, and utilize an approximation of the spectra of horizontal velocity ( $\Phi_u$ ) as a function of vertical wavenumber ( $\kappa_z$ ):

$$\Phi_u(\kappa_z) = \begin{cases} \frac{2}{3} \epsilon^{\frac{2}{3}} \kappa_z^{\frac{5}{3}} q(k) & \kappa_z \geq \kappa_o & Ri < \frac{1}{4} \\ \frac{2}{3} N^2 \kappa_z^{-3} & \kappa_z \leq \kappa_o & Ri = \frac{1}{4} \end{cases} \quad (8)$$

where we identify:  $\kappa_z = \frac{1}{l_*}$ ,  $k = \frac{\kappa_z}{\kappa_v}$ ,  $q(k) = \frac{1}{1+(3.2k)^{3.7}}$ ,  $\kappa_v = \frac{1}{\eta} = (\frac{\epsilon}{\nu^3})^{\frac{1}{4}}$ ,  $\kappa_o = \frac{1}{L_o} = (\frac{\epsilon}{N^3})^{\frac{1}{2}}$ .

Equation 8(a) is the classical isotropic turbulence ocean 1D spectral model, first introduced by Nasmyth (1970). Equation 8(b) is the spectra of the anisotropic turbulent buoyant subrange model and follows the form introduced by Avsarkisov (2020).

In Figure 3 we show  $\Phi_u(\kappa_z)$ , given in Equation 8 (a, b), for the case of  $N = 0.01 \text{ s}^{-1}$ . Note that increasing the value of N shifts the magnitude of the spectra of the buoyant subrange to larger values, and vice versa. The color coded squares in Figure 3 indicate the location of the Ozmidov scale,  $L_o$ , the smallest length scale of the buoyant subrange, and, thus, the largest length scale of the inertial subrange for various values of  $\epsilon$ , as indicated in Figure 3, and which spans a typical range of oceanographic values. It should also be noted that these squares represent the boundary of  $Ri = \frac{1}{4}$ . Below and to the left of this boundary, stratification dominates in what is commonly referred to as the buoyant subrange, where the turbulence cascade is horizontal only (Avsarkisov, 2020). Above and to the right of this boundary is the inertial subrange, where

turbulence is isotropic and fully three-dimensional. It is important to point out that the spectra of Equation 8 (a, b) is an idealization, with the boundary of  $Ri = \frac{1}{4}$  an approximation but with  $\Delta Ri \ll Ri = \frac{1}{4}$ .

For Figure 3 we have chosen to set the layer thickness  $h = 10\text{m}$ , or equivalently  $\kappa_z = 0.1 \text{ m}^{-1}$ . However, the spectra of Figure 3 can also be used for cases  $(l_*)_{min} < l_* < h$ , where  $(l_*)_{min} = \frac{1}{(\kappa_z)_{max}}$  is indicated by the black square in Figure 3.

Stability can now be defined through the location of the forcing in wavenumber space, namely, when  $\kappa \geq \kappa_c$ , and, in real space, when  $l_* \leq l_c$ , with  $\kappa_c = \frac{1}{l_c}$  representing the outer wavenumber boundary of the inertial subrange, where viscosity begins to play a dominant role over inertial effects.

As a first approximation, let  $l_c = \gamma \eta$ , or equivalently,  $\kappa_c = \frac{\kappa_v}{\gamma}$ . The large filled circles are values of  $\kappa_c$  for  $\gamma = 10$ , a common oceanographic approximation, which represents instability occurring at values of  $l_c$  that are a decade larger than the Kolmogorov length scale,  $\eta$ , shown in Figure 3 as the small filled circles. Clearly Figure 3 shows that with  $\gamma = 10$ ,  $\kappa_c$  is located at the end of the inertial subrange of  $\Phi_u(\kappa_z)$ . The region below and to the right of these circles represents the dissipative zone. In this region the cascade of turbulence originating at larger scales is arrested (leading to dissipation to heat at the Kolmogorov scale). Most importantly for our purposes here, forcing at these scales will be damped and will not grow, such that  $l_c$  may be intrinsically related to the gradient scale. We now relate  $l_c$  (and/or  $\kappa_c$ ) directly to viscosity.

First, note that in the inertial subrange we can use the approximation

$$(u_*)^2 = \epsilon^{\frac{2}{3}} l_*^{\frac{2}{3}} \quad (9)$$

which represents the integration of the spectra in Equation 8, and yields the  $u_*$  value consistent with a given turbulent field.

Alternatively, using the definition of  $\bar{S}$ ,

$$(u_*)^2 = \frac{1}{4} \bar{S}^2 l_*^2 \quad (10)$$

Combining Equations 9, 10 implies that

$$\varepsilon = \frac{1}{8} \bar{S}^3 l_*^2 \quad (11)$$

Considering turbulent eddies at the critical scale, we can assume that  $l_* = l_c$ . Returning to the relationship  $l_c = \eta \gamma$ , then substituting the definition of  $\eta$ , leads to (11) being transformed as  $l_c = \gamma \left( \frac{8\varepsilon}{\bar{S}^3 l_c} \right)^{\frac{1}{2}}$ . Rearranging to solve for  $l_c$  yields:

$$l_c = \sqrt{2} \gamma^{\frac{2}{3}} l_s \quad (12)$$

where  $l_s = \left( \frac{\nu}{S} \right)^{\frac{1}{2}}$ . We refer to  $l_s$  as the primitive shear length scale, by analogy to the primitive length scale,  $l_p = \left( \frac{\nu}{N} \right)^{\frac{1}{2}}$ , which has been considered in the literature in comparison to  $L_o$  (Imberger, 1994; Saggio and Imberger, 2001), and represents the scale at which the effects of stratification are comparable to viscosity. Thus,  $l_s$  characterizes the balance between shear and viscosity, and represents the length scale for which  $Re = 1$  for a given shear. Assuming  $\gamma \approx 10$ , then  $l_c \approx 7l_s$ . Instabilities below this scale are unlikely to develop into turbulence due to the stabilizing influence of viscosity, and thus, a value of  $\sim 10l_s$  conceivably represents the gradient scale, or the lower end of the range where the critical value of  $Ri = 1/4$  is valid.

## 2.1 An energetics approach

An alternative approach to the derivation of  $l_s$  follows from an expanded version of the energetics analysis defining the critical value of  $Ri_g$  as  $1/4$  provided by Drazin and Reid (1981), and Chandrasekhar (1961). The Drazin and Reid (1981) argument is based on balancing the work required to affect the exchange of two water parcels in the vertical,  $\delta W = -g\delta\rho\delta z$ , with the kinetic energy released during the process,  $\delta T \leq \frac{1}{4}\rho(\delta U)^2$  (assuming that the exchange occurs over a small enough vertical distance that the inertial effects of buoyancy on the release of kinetic energy are negligible). Here, the work required is simply the amount necessary to account for the gain in potential energy. Now consider an extension to this argument, recognizing that, at very small scales, the work required to affect the change in the vertical must also be sufficient to overcome the influence of molecular viscosity. Through scaling, and by analogy to the definition of the turbulent eddy viscosity as  $\nu_e \sim \frac{p}{S}$ , we define a loss term due to molecular viscosity as  $\delta T_{Loss} = \nu\rho S$ , such that a modified version of the Drazin and Reid (1981) argument can be written as:

$$\delta W \leq \delta T - \delta T_{Loss} \quad (13)$$

or, expanded, as:

$$-g\delta\rho\delta z \leq \frac{1}{4}\rho(\delta U)^2 - \nu\rho S \quad (14)$$

The molecular viscosity term becomes negligible when  $\frac{\nu\rho S}{\frac{1}{4}\rho(\delta U)^2} \ll 1$ , leading to  $\delta z \gg 2\left(\frac{\nu}{S}\right)^{\frac{1}{2}} = 2l_s$ , assuming that  $\delta U = S\delta z$ . Recognizing that  $\delta z$  in this case is consistent with the gradient

scale (i.e., the low end of the valid gradient Richardson number range), this result is consistent with (12) given the conventionally accepted value of  $\gamma \sim 10$ , and assuming the gradient scale lies somewhere near the limit of the interial subrange.

While the Kolmogorov lengthscale,  $\eta$ , and  $l_s$  both represent the effects of molecular viscosity on turbulence,  $\eta$  represents viscous effects on the dissipation of turbulence, where  $l_s$  may be better suited for understanding the effect of viscosity on the initiation of turbulence. Furthermore,  $\eta$  cannot be determined without *a priori* knowledge of the turbulent field and the TKE dissipation rate, whereas  $l_s$  can be calculated strictly with bulk flow variables, making it much more practical in a predictive capacity.

A representative value of shear in an energetic river plume environment (e.g., MacDonald and Geyer, 2004, Fraser River; MacDonald et al., 2007, Merrimack River; McCabe et al., 2008, Columbia River) is on the order of 0.3 - 0.5 s<sup>-1</sup>, leading to  $l_s$  on the order of 1-2 mm. For comparison, in the same environments, Kolmogorov scales are typically an order of magnitude smaller. In the much larger scale Mediterranean overflow, a representative value of  $\bar{S}$  on the order of 0.01 s<sup>-1</sup> (Baringer and Price, 1997) yields  $l_s$  on the order of a cm, in this case comparable to values of the Kolmogorov scale in the same environment. In neither of these cases can typical observations produce Richardson number estimates at scales approaching the gradient scale, which would require vertical resolution on the order of  $\sim 10l_s$  or smaller. Observations in river plume environments typically yield velocity profiles at no better than 25 cm resolution in the vertical, and density profiles with resolutions on the order of cms to tens of cms. Larger scale ocean observations are likely to resolve velocity profiles only at scales of meters or higher. Thus, it is unlikely that standard ocean observing techniques are ever capable of resolving Richardson numbers at the gradient scale.

It is useful to consider the value of  $l_s$  in the context of the overall shear stratified layer thickness,  $h$ , resulting in a dependency on the overall layer Reynolds number,  $Re$ .

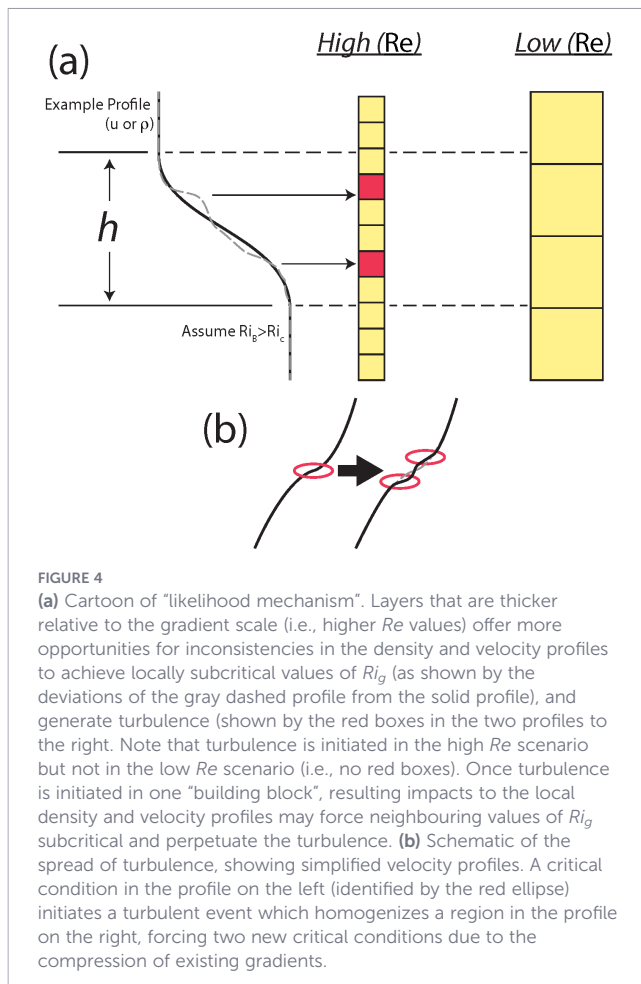
$$\frac{h}{l_s} = \frac{S^{\frac{1}{2}}h}{2\nu^{\frac{1}{2}}} \approx \frac{(\Delta U)^{\frac{1}{2}}h}{2\nu^{\frac{1}{2}}h^{\frac{1}{2}}} = \frac{(\Delta U)^{\frac{1}{2}}h^{\frac{1}{2}}}{2\nu^{\frac{1}{2}}} = Re^{\frac{1}{2}} \quad (15)$$

Note that here we approximate  $S$  as  $\frac{\Delta U}{h}$ , representing the average shear across the layer. Clearly, small variations in shear across the layer could result in a modification of the  $l_s$  scale locally throughout the layer, but (15) illustrates the utility of the layer Reynolds number in representing the thickness of the layer as a function of the primitive shear scale, or more importantly, the gradient scale.

## 2.2 The "likelihood mechanism"

As pointed out above, conventional ocean measurement techniques are rarely, if ever, adequate to constrain velocity and density profiles at scales on the order of  $10l_s$ . Thus, there may be no direct way to evaluate the importance of this scale to the development of turbulence, particularly in larger scale geophysical flows. However, we can address this issue by considering the following:

The definition of  $Ri_B$  in (2) essentially represents a larger scale perspective of  $Ri_g$ , or a ratio of the mean gradients across the entire



shear layer thickness,  $h$ . However, due to natural fluctuations and perturbations related to layering, secondary interfaces, and residual turbulence, the value of  $Ri_g$  everywhere is not expected to equal  $Ri_B$ . Riley and de Bruyn Kops (2003) have discussed the importance of subcritical  $Ri_g$  values at some point within the larger structure of a stratified flow in generating turbulence. Similarly, Caulfield (2020, 2021) has suggested that spatiotemporal variability in  $Ri$  makes it very challenging to characterize any flow as “highly stratified”. Thus, we consider a “likelihood mechanism” to represent the possibility that any subrange within the shear layer at appropriate gradient scales (i.e.,  $\sim 10 l_s$ ) might meet the critical criteria of  $Ri_g < \frac{1}{4}$ . As the thickness of the shear layer increases relative to the gradient scale, consistent with increasing values of  $Re$  as illustrated in (5), the likelihood that a critical condition occurs somewhere in the layer should also increase, as suggested by the variability illustrated in Figure 2 and the schematic shown in Figure 4a. Conversely, as the value of  $Ri_B$  increases, it becomes less likely that isolated regions of  $Ri_g$  would fall below the critical value of  $\frac{1}{4}$ .

Once a local instability has been triggered within the shear layer, turbulent processes will work towards homogenizing the fluid across a patch with a vertical length scale of order  $L_o$ , resulting in decreased shear and stratification, and generally increasing local values of  $Ri_g$  within the patch. However, at the top and bottom edges of this patch, gradients must increase, in order to match the existing density and velocity profiles outside the patch (as shown in

Figure 4b), with a corresponding decrease in local  $Ri_g$ . In many cases, this strengthening of gradients will force these regions into a locally subcritical condition, resulting in the spread of turbulence throughout the shear-stratified layer. In this manner, turbulence from a single instability may spread, similar to a single spark ultimately leading to a large inferno. However, this spread of turbulence is likely to be damped for larger values of  $Ri_B$  if the gradients at the patch edges are not sufficiently increased to reach a subcritical condition, so that even at high  $Re$  values, some flows may remain stable.

In Section 3.0, we test these hypotheses by evaluating flows across a broad range of  $Re$  values to evaluate the presence of turbulence at higher values of  $Ri_B$  as a function of  $Re$ . This approach can be used to empirically constrain the upper limit of the gradient range.

### 3 Constraining the gradient range

Given the inadequacy of conventional oceanographic measurements to directly observe variability at scales on the order of  $10 l_s$ , we utilize an inferred approach based on the proposed likelihood mechanism. First, we establish a common framework for comparing a wide variety of laboratory and observational data, followed by a direct comparison of turbulence intensity across a range of  $Re$  values.

#### 3.1 Velocity scales and interfacial drag

To normalize and compare data across a wide array of laboratory experiments and observational studies, we utilize a modified interfacial drag coefficient, as a common currency of turbulence:

$$C_{Di} = \left( \frac{u_*}{\Delta u} \right)^2 \quad (16)$$

with  $u_* = \left( \frac{\tau}{\rho} \right)^{\frac{1}{2}}$  representing the shear velocity, or outer scale turbulent velocity. Here  $\tau$  represents a turbulent interfacial stress. We choose this parameter for its simplicity as a comparison of turbulent to bulk fluid velocities. Note that  $C_{Di}$  is also functionally equivalent to a non-dimensional form of the eddy viscosity,  $\frac{\nu_T}{h\Delta u}$ , related to a non-dimensional form of the TKE dissipation rate,  $\frac{\epsilon}{\Delta u g^T}$  (MacDonald and Geyer, 2004), and is often used in studies of oceanographic turbulence (e.g., Burchard and Rippeth, 2009; Jurisa et al., 2016). A second turbulent velocity scale, the entrainment velocity,  $w_e$ , is also often found in the literature, particularly in earlier laboratory studies, where an entrainment coefficient is typically defined as  $E = \frac{w_e}{\Delta u}$ . In many cases, researchers have assumed that the entrainment velocity scales with the turbulent velocity such that  $u_* \sim w_e$  (e.g. Wells et al., 2010; Strang and Fernando, 2001), as entrainment and turbulence are related processes. However, the entrainment process represents one-way transport of fluid across a defined boundary, while the turbulent velocity scale represents a balanced exchange of fluid (MacDonald

and Geyer, 2004), and thus, these two parameters may differ substantially (e.g. Price, 1979), as expressed by their ratio,  $a_* = \frac{u_*}{w_e} = \frac{C_{Di}}{E}^{\frac{1}{2}}$ .

We reduce data from a variety of sources to values of  $C_{Di}$ ,  $Ri_B$ , and  $Re$  for comparison. In cases where TKE dissipation rates,  $\varepsilon$ , are reported, we use the following relationship, after Ivey and Imberger (1991) and MacDonald and Geyer (2004):

$$C_{Di} = \frac{Ri_B}{(1 - Ri_f)} \frac{\varepsilon}{g' \Delta u} \quad (17)$$

$Ri_f = \frac{P}{\rho}$  represents the ratio of the buoyancy flux term to the shear production term in the TKE equation.

$Ri_f$  is often assumed constant at a value of approximately 0.18 to 0.2 (Gregg et al., 2018) for stratified shear flows, particularly in the analysis of field observations where observed ratios are driven by the net impact of many individual turbulent events. Although DNS evidence suggests that  $Ri_f$  can vary substantially throughout the evolution and decay of a single Kelvin Helmholtz billow (Smyth et al., 2001; Salehipour and Peltier, 2019) we follow Gregg et al. (2018) here, and focus on the integrated effects of many billows resulting in net mixing in the ocean environment. However, a decreasing value of  $Ri_f$  under conditions of very low stratification, and thus decreasing  $Ri_B$ , must be accounted for (e.g., Balmforth et al., 1998; Peltier and Caulfield, 2003; Venayagamoorthy and Koseff, 2016), as stratification is necessary for the conversion of TKE to potential energy, and support a buoyancy flux as a sink of TKE. Here, we represent the value of  $Ri_f$  by a simple empirical expression to parameterize this decay for very low values of  $Ri_B$ :

$$Ri_f = 0.18(1 + 0.01Ri_B^{-2})^{-1} \quad (18)$$

This approximation is restricted to naturally occurring turbulence in stratified shear flows generated through KH instabilities. It should be emphasized that the exact nature of  $Ri_f$  variability, particularly at the single overturn scale, remains a subject of open scientific debate (e.g. Lozovatsky and Fernando, 2013), and may ultimately depend on the organization of locally critical turbulent patches within the larger flow structure (e.g., Salehipour et al., 2018; Smyth et al., 2019). However, given the focus of the present analysis on net mixing processes, the parameterization in (7) provides an effective means of addressing the issue of mixing efficiency.

Entrainment rates reported in the literature are reduced by using the relationship

$$C_{Di} = (Ea_*)^2 \quad (19)$$

where  $a_*$  is parameterized as (e.g. Christodoulou, 1986; Kato and Phillips, 1969; Pollard et al., 1973; Price, 1979):

$$\begin{aligned} a_* &= c_1 Ri_B & Ri_B > \sim 10^{-1} \\ a_* &= c_2 Ri_B^{\frac{1}{2}} & Ri_B < \sim 10^{-1} \end{aligned} \quad (20)$$

and values of  $c_1$  and  $c_2$  are on the order of 50 and 16, respectively. Unlike  $C_{Di}$  and  $E$ ,  $a_*$  is a ratio of two turbulent scales and does not incorporate any bulk flow scales in its definition. Thus, we

hypothesize that (20) adequately expresses the empirical variability in  $a_*$ , suggesting that (20) is consistent across large ranges of  $Re$ , which has been supported by observations at higher  $Re$  values (e.g., MacDonald and Geyer, 2004).

### 3.2 Comparison of existing data

The panels in Figure 5 show turbulence data from a variety of sources, including both laboratory and field data, reduced to  $C_{Di}$  and plotted as a function of  $Ri_B$ . The data is segregated by  $Re$  value, with  $Re > 5 \times 10^5$  ( $\frac{h}{l_s} > 700$ ) shown in panel (a) and  $Re < 2 \times 10^4$  ( $\frac{h}{l_s} < 140$ ) shown in panel (b). Data represented includes the compiled data utilized by Christodoulou (1986) transformed to  $C_{Di}$  using (19) and (20). This data is referred to as “Legacy Data” in the legend, and  $Re$  has been approximated for most of this data (i.e., Ellison and Turner, 1959; Chu and Vanvari, 1976; Pedersen, 1980; Buch, 1980) based on estimates of length and velocity scales inferred from the original manuscripts based on the size of the experimental apparatus or observational context. In these cases, a single representative value has been assigned for each data set. While these estimates are only representative, the likely error in this approach is small compared to the  $Re$  parameter space spanning more than five orders of magnitude.

Data has also been drawn from field studies referenced in Wells et al. (2010) and Cenedese and Adduce (2010), with certain studies (e.g., Girton and Sanford, 2003; Peters and Johns, 2005; Arneborg et al., 2007) removed due to the influence of bottom boundary layers. Likewise, the laboratory data of Cenedese and Adduce (2008) has not been included due to the potential for bottom boundary layer influence. Data from a range of unbounded shear stratified flows, including several river plume studies (e.g., MacDonald and Chen, 2012; MacDonald et al., 2007; Kilcher et al., 2012), and laboratory data from Yuan and Horner-Devine (2013) have also been added. Note that small scale stratified shear layers are represented in Figure 5 exclusively by laboratory data. DNS studies, which cover a similar parameter space to laboratory studies often focus primarily on the internal dynamics of KH billows or similar instabilities, and rarely report mean, or net, turbulent quantities. DNS results can also be highly sensitive to initial and boundary conditions (Palma et al., 2024), and thus may not always be directly comparable to naturally occurring flows.

The plots in panels (a) and (b) provide an interesting segregation of the data. At low  $Re$  values (panel b),  $C_{Di}$  is observed to peak near  $Ri_B \approx \frac{1}{4}$ , with a subsequent decay for increasing values of  $Ri_B$ . For high  $Re$  values (panel a), no such decrease is seen, with  $C_{Di}$  values remaining consistently high as  $Ri_B$  increases. The range of  $Re$  in panel (a) is clearly above the higher limit of this gradient range, whereas the data in panel (b) likely bridges the upper end of the gradient range. In particular, the data of Pedersen (1980), which lies at the high end of the  $Ri_B$  range in panel (b) also represents the highest  $Re$  values in that range. The scatter observed in  $C_{Di}$  for this data is consistent with our proposed mechanism, suggesting that this  $Re$  range represents an intermediate layer thickness that will only periodically decay to turbulence, and thus, exists right on the edge, statistically, of turbulent extinction for supercritical  $Ri_B$  values. The appropriate

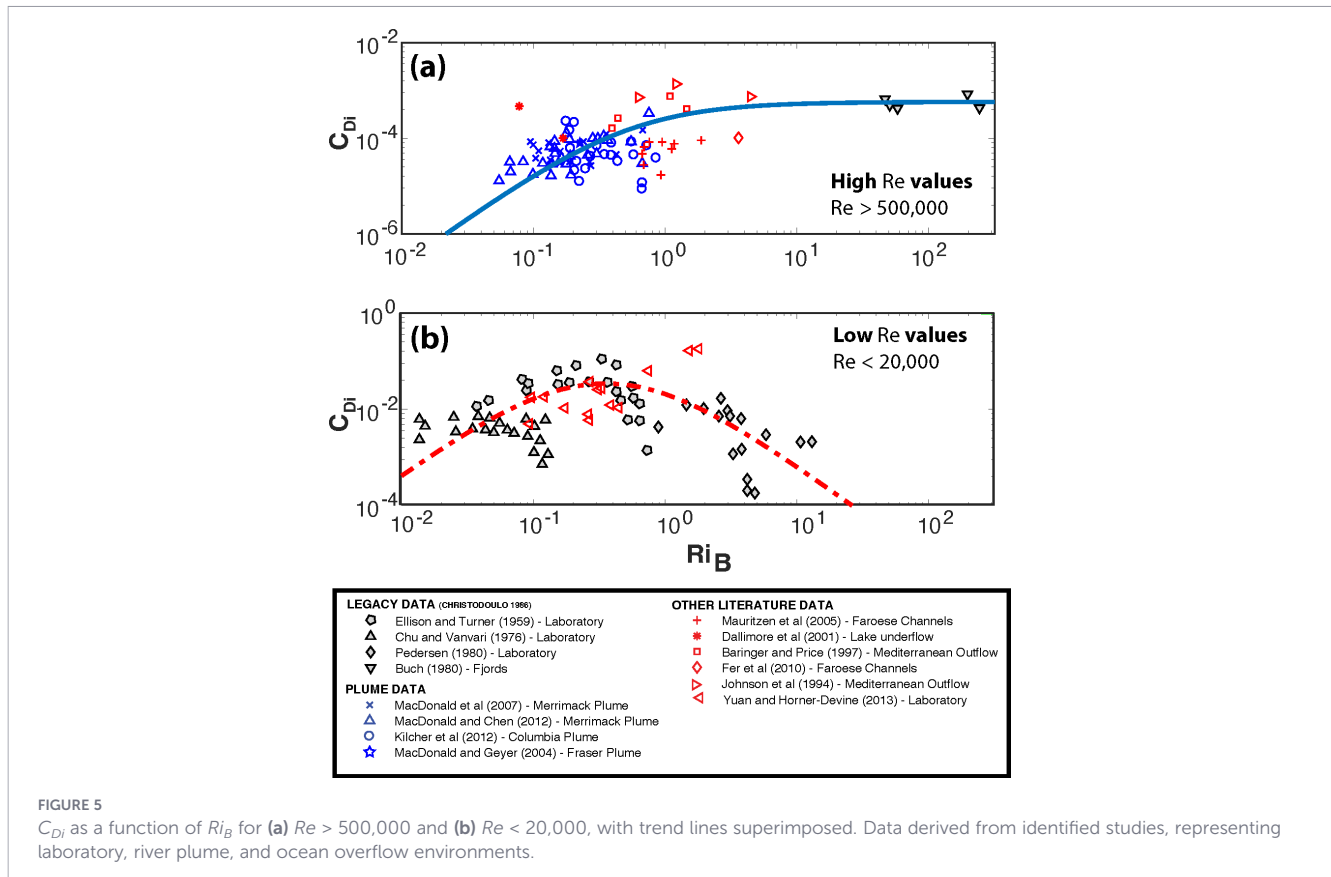


FIGURE 5

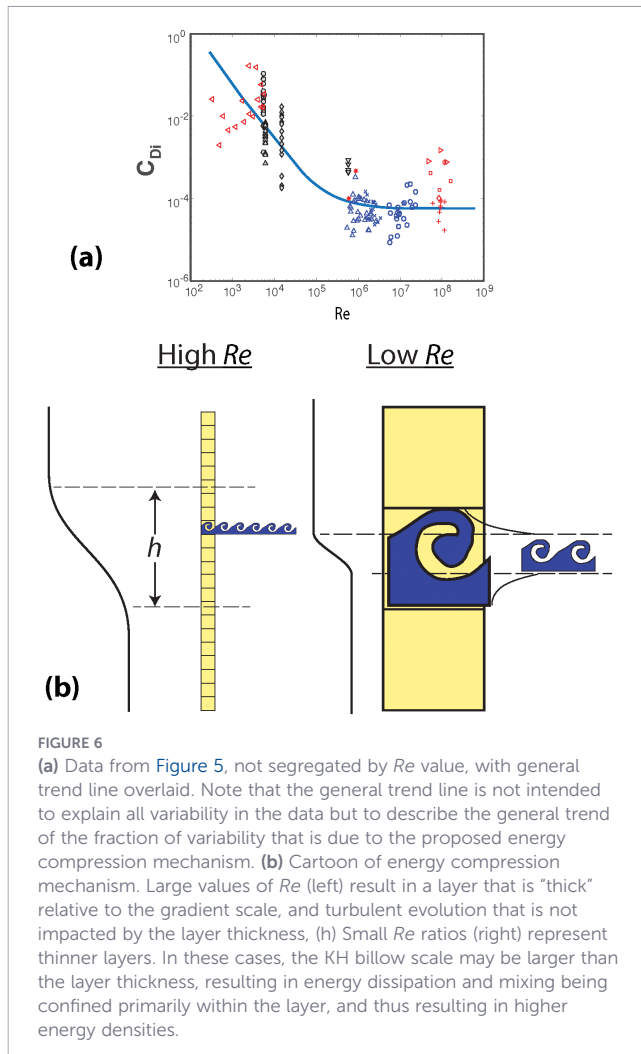
$C_{Di}$  as a function of  $Ri_B$  for (a)  $Re > 500,000$  and (b)  $Re < 20,000$ , with trend lines superimposed. Data derived from identified studies, representing laboratory, river plume, and ocean overflow environments.

upper end of the gradient range likely falls somewhere below the upper limit of  $Re = 2 \times 10^4$  (i.e.,  $\frac{h}{l_s} = 140$ ) in panel (b). Thus, the gradient range likely extends from  $\sim 10 l_s$  ( $Re \sim 100$ ) to somewhere less than  $100 l_s$  ( $Re \sim 10^4$ ). Near the higher end of this range, as suggested by the Pedersen data, the shear layers only intermittently produce turbulence at supercritical values of  $Ri$ . At significantly higher values (e.g.  $10^3 l_s$  or  $Re > 10^6$ ) layers will consistently sustain turbulence at supercritical (i.e.,  $> 1/4$ ) values of  $Ri$ . In theory, the likelihood mechanism would suggest that there will always exist a high end  $Ri_B$  value at which turbulence will roll off, at a point when the density gradient provides such strong stability that subcritical  $Ri$  values are not likely to occur even across small ranges within the layer consistent with the gradient scale. However, in practice, the roll off  $Ri_B$  value may be sufficiently high once layer thicknesses exceed 100–1000 times the gradient scale, that it is essentially unrealistic, yielding most oceanographic shear stratified layers of sufficient thickness vulnerable to turbulent mixing, regardless of stratification.

In both panels,  $C_{Di}$  decreases for small values of  $Ri_B$ , which is expected due to the decreased importance of stratification in these environments (Forryan et al., 2013). Although unstratified, or minimally stratified, fluids are easily mixed, it is this relative ease of mixing that can result in the potentially counterintuitive result of decreased turbulence. Relatively rapid homogenization of the fluid will eliminate the velocity shear necessary to generate turbulence, unless the shear is forced by a boundary layer such as an imposed wind stress, or a no-slip condition along a bottom boundary. Additionally, turbulence in the limit of low

stratification may be substantially less energetic because it does not have to overcome the potential energy constraints of the density gradient.

Another striking difference in Figures 5a, b is the relatively more intense turbulence, when expressed as  $C_{Di}$ , observed at low  $Re$  values (panel b), as compared to high  $Re$  values in panel (a). This phenomenon has been observed in other recent efforts to quantify the difference between DNS and geophysical scale turbulence, and is discussed in more detail in Section 4. Without considering the effect of  $Re$ , several previous studies have attributed the reduced intensity of turbulence in geophysical scale flows to other mechanisms. For example, Christodoulou (1986), grouped the fjord data of Buch (1980), the inverted triangles in Figures 5a, with laboratory and other low  $Re$  flows, to illustrate the roll off of turbulence at high  $Ri_B$  values. Cenedese and Adduce (2010) suggested a positive correlation between  $Re$  and  $E$ , such that higher  $Re$  flows would be generally associated with higher entrainment. However, the data set explored in Cenedese and Adduce (2010) contained only a limited amount of field data at high  $Re$ , including several experiments which may have had significant bottom boundary layer influence. Furthermore, the represented field data in Cenedese and Adduce (2010) is biased towards higher values of  $Ri_B$ , with no observations of ocean scale flows at subcritical  $Ri_B$  values, similar to Christodoulou (1986). Thus, the decrease in turbulence observed by Cenedese and Adduce (2010) for geophysical scale observations, which they attributed to supercritical  $Ri_B$  values in their parameterization, may, in fact, be attributable to the high  $Re$  values associated with these flows. The key distinction between



these earlier studies and this analysis is the inclusion of a preponderance of data from river plume environments, which exhibit high  $Re$ , low  $Ri_B$  flows, enabling a more complete assessment of the nature of turbulence occurring at high  $Re$  values (i.e., panel (a) in Figure 5).

## 4 Discussion

In previous sections we have constrained the gradient range to between  $\sim 10 l_s$  and  $\sim 100 l_s$ , introduced the concept of the Likelihood Mechanism, and observed reduced turbulent intensity with increasing  $Re$ , all of which may have important implications for the understanding of turbulence as a function of bulk flow quantities in geophysical settings. In this section, we first undertake a more detailed assessment of the observed decrease in turbulence intensity with increasing  $Re$ , followed by insight into a new approach for parameterizing shear stratified turbulence as a function of both  $Ri_B$  and  $Re$ , and finally, conclude with some considerations on the relevance of a critical value of  $Ri_B$ .

### 4.1 Amplification of turbulence at low $Re$

As demonstrated in Figure 5, lower  $Re$  flows typically exhibit higher values of  $C_{Di}$  compared to higher  $Re$  environments. This phenomenon of turbulence amplification at low  $Re$  can also be seen directly in Figures 6a, where all the collected data is plotted as  $C_{Di}$  vs.  $Re$ . Keep in mind when evaluating this figure that a significant amount of variability in  $C_{Di}$  can be attributed to  $Ri_B$ , which is not represented on either axis. Nevertheless, amplification of  $C_{Di}$  is apparent for  $Re < 10^3$ .

Recent efforts to quantify the difference between DNS and geophysical scale turbulence as the result of continuous (in the geophysical case) vs. intermittent (in the DNS case) forcing mechanisms (e.g., Holleman et al., 2016; Zhou et al., 2017), provide a ready mechanism to explain the observed amplification. Consider a growing instability in a low  $Re$  environment, characterized by a relatively thin (i.e., a relatively low  $\frac{h}{l_s}$ ) shear stratified layer. In such a layer, the instability will be subjected to a temporally varying stress profile as it expands beyond the limits of the stratified shear region into unstratified (and/or unstratified) fluid above and below the layer. In contrast, in a high  $Re$  flow, generated instabilities are wholly embedded in a uniform shear layer, and thus subject to a more continuous forcing profile throughout their evolution and decay. This essentially results in an “energy compression” mechanism for low  $Re$  flows. In these cases, growth of turbulent billows into the unstratified regions above and below the stratified shear layer is not opposed by background density gradients or shear, so that most of the energy in the billow collapses back into the shear layer, resulting in an increased energy density within the shear layer. In regions of high  $Re$ , the growing billows are not influenced by the stratified shear layer boundaries, and the energy is distributed more broadly. This energy compression mechanism is illustrated in Figure 6b.

### 4.2 Insight towards a $Ri_B - Re$ turbulence parameterization

At sufficiently high values of  $Re$ , we expect that both the Likelihood and Energy Compression mechanisms are saturated, in that the layer has reached a minimum thickness for sustaining turbulence at supercritical values of  $Ri_B$ , as well as providing ample vertical breadth to prevent the layer boundaries from resulting in any energy compression effects. Within such  $Re$  environments,  $Ri$  values are the primary driver of stratified shear turbulence dynamics.

However, in flow regimes characterized by low to intermediate  $Re$  values,  $Re$  may play an important role. These impacts may become increasingly important for analysis of DNS and laboratory flows, and particularly to the comparison of these flows to larger scale geophysical flows. To better assess and visualize these potential impacts we have developed an empirical parameter space mapping of  $C_{Di}$  based on the collected data and empirical representations of the Likelihood and Energy Compression mechanisms. Details of the empirical approach are given in the Appendix. The new parameter space mapping provides an approximate and representative surface

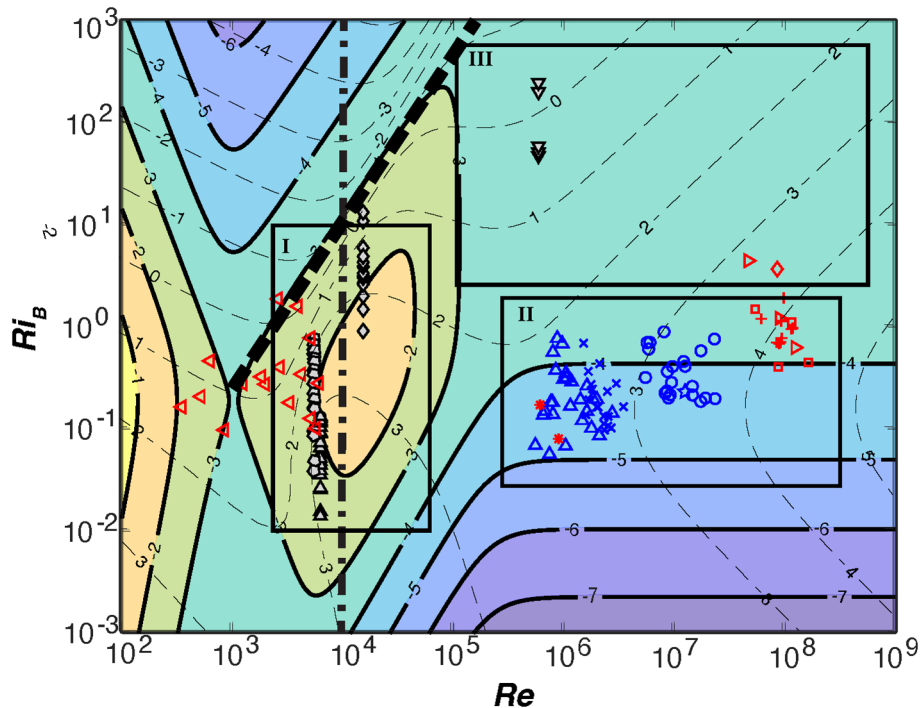


FIGURE 7

Contours of  $C_{Di}$  (solid) in the  $Ri_B - Re$  plane, calculated via the approach described in detail in the Appendix. Dashed contours represent the value of  $Re_b = \frac{h}{\sqrt{N^2}}$  (based on bulk flow variables). Data from Figure 5 is overlain to indicate distribution of data in the  $Ri_B - Re$  plane. The gradient range exists at the left edge of the figure, from the gradient scale at  $Re = 100$  to the upper edge of the gradient range at  $Re = 10^4$ , shown by the bold dash-dot line. The bold dashed line represents an approximation of “critical”  $Ri_B$  value as a function of scale. Rectangular boxes labelled I, II, and III represent specific dynamical regions, as described in the text. See Figure 5 for data legend.

of turbulence intensity in the  $Re - Ri_B$  plane, as shown in Figure 7, where contours of  $C_{Di}$  are plotted as solid contours. It should be noted that Salehipour et al. (2016b) describe a multi-dimensional parameterization for the turbulent mixing efficiency in terms of  $Ri_g$  and  $Re_b$ , similar in some respects to the effort undertaken here. However, their parameterization does not address the overall scale of the stratified shear layer. Here, the overall layer thickness,  $h$ , is considered a key parameter in setting the turbulence intensity, as described by  $C_{Di}$ . For reference, contours of  $Re_b$  are also overlain on Figure 7, and little consistency between contours of  $C_{Di}$  and  $Re_b$  is noted.

Several interesting regions and effects can be recognized in Figure 7. The peak in  $C_{Di}$  near  $Ri_B \approx \frac{1}{4}$  and  $Re \approx 10^4$ , labeled as Region I in Figure 7, is the focus of most laboratory and DNS experiments. This region represents an optimal balance of stratification and shear, coupled with a sufficiently low layer thickness for turbulence amplification, to achieve maximal turbulent energetics.

At higher values of  $Re$  ( $> \sim 10^5$ ) we observe the majority of the field-based data, clustered near the top of a steep slope (Region II), which falls off to low  $C_{Di}$  values for low values of  $Ri_B$ . Along this slope, we see that the data is distributed with more coastal and estuarine field sites, including the MeRMADE (e.g. MacDonald et al., 2007) and RISE (e.g. Kilcher et al., 2012) plume studies as well as saline lake underflows (Dallimore et al., 2001), lying at the low end of this  $Re$  range and larger scale deep ocean overflows, including the Mediterranean (Johnson et al., 1994; Baringer and Price, 1997) and Faroes (Mauritzen et al., 2005; Fer et al., 2010)

overflows, occupying the higher end. Note that above a value of  $Re \approx 10^6$ ,  $C_{Di}$  becomes primarily a function only of  $Ri_B$ , as has been long reflected in turbulence closures (e.g. Burchard and Baumert, 1995; Umlauf and Burchard, 2003; Canuto et al., 2010) for ocean models. This region is reflective of the conditions across most of the unbounded stratified shear flows within the world’s oceans, where  $Ri_B$  values cluster near  $\frac{1}{4}$  due to inherent feedback mechanisms controlling turbulent evolution, and the shear layer is thick enough that it places no constraints on turbulent processes. The feedback processes driving  $Ri_B$  to near a value of  $\frac{1}{4}$  have been described in the context of marginal instability (Thorpe and Liu, 2009; Smyth and Moum, 2013; Howland et al., 2018), an equilibrium between forcing mechanisms driving increased velocities (and lower  $Ri_B$ ), and turbulence, which reduces velocity gradients and drives  $Ri_B$  values higher.

Above this slope, the analysis suggests a broad plateau (Region III), where high  $Ri_B$  values dominate across thick shear layers, but turbulence persists due to initiation by localized regions of subcritical  $Ri_g$ . This region is characterized by a scarcity of data, with the exception of Fjord data (Buch, 1980), and the upper limits of the ocean overflow data at the very top of Region II.

The left edge of Figure 7 represents the gradient scale at  $Re = 100$  ( $\frac{h}{l} \sim 10$ ), while the bold dashed-dot line at  $Re = 10^4$  ( $\frac{h}{l} \sim 100$ ) represents the approximate upper limit of the gradient range discussed above. A steep increase in  $C_{Di}$  is observed for very thin stratified shear layers approaching the gradient scale from higher  $Re$  values. Although the contours near the gradient scale should be viewed with extreme caution, due to the lack of data in the region, a

dichotomy of flows in this region might be expected. The region with low  $Re$  and high  $Ri_B$  (upper left corner) would be characterized primarily by a small velocity gradient and a small to mid-range layer thickness. In this region, stability, and a lack of turbulence, would be expected. Conversely, the region with low  $Re$  and low  $Ri_B$  (lower left corner) would generally represent conventional two-layer flows, where the boundary between the two water masses is exceedingly narrow, and the influence of the “energy compression” mechanism is maximal. Flows in this actively turbulent region would be necessarily transient, however, with rapid mixing thickening the gradient zone, and forcing the flow to migrate across the turbulent landscape towards equilibrium conditions as suggested by the preponderance of data near Region I and the top of Region II. In this regard, it should be noted that any flow may be migratory, as the effects of mixing modify the environment and thus alter both  $Ri_B$  and  $Re$ . In many cases, the natural environment and forcing mechanisms may result in the flow converging towards one of the equilibrium zones in Regions I, II, or III, and ultimate maintenance of a “marginal instability” environment. In others, initial stratification may be erased by mixing, resulting in a migration of the flow down the Region II slope towards vanishingly small values of  $Ri_B$ , where the water column becomes homogenized and stratified shear turbulence is not supported.

The parameter space shown in Figure 7 encompasses most of the world’s ocean environments, down to laboratory scale flows. Most oceanic flows above a  $Re$  of approximately  $10^5$  or  $10^6$  are well characterized by existing  $Ri$  based turbulence parameterizations, as indicated by the lack of sensitivity to  $Re$  above this range. However, flows with  $Re$  on the order of  $10^5$  or smaller may be poorly characterized by these parameterizations. This may include time-dependent, developing flows, such as the growth of the stratified shear region transitioning the ocean mixed layer (e.g., Giunta and Ward, 2022) to deeper water masses, particularly during seasonal transitions, or smaller scale flows in estuaries or embayments where layer thicknesses are constrained (e.g., Matsumoto and Nakayama, 2024). In these environments, traditional parameterizations may substantially underestimate TKE and thus underpredict the growth and/or mixing associated with these flows. At yet smaller scales (e.g.,  $Re$  of  $10^4$  or less), approaching the scale of laboratory flows, buoyant runoff from tidal flats into the main channels of estuaries may exhibit substantially higher mixing than would be otherwise predicted. Perhaps most importantly, given that the flows above are limited in scope, the parameter space shown in Figure 7 may yield significant insight into the use of DNS (e.g. Mashayek et al., 2017) or laboratory scale investigations (e.g. Yuan and Horner-Devine, 2013) to predict turbulent behavior at much larger values of  $Re$ .

### 4.3 A critical value of $Ri_B$

As discussed in Section 1.0, relatively arbitrary values are generally selected for a critical value of  $Ri_B$ , with a value of 0.5 to 1.0 often taken as a default. The present work provides more refined insight into this important question, and points towards a clear dependence on scale. Given the parameterization presented in Figure 7, a reasonable expectation for the critical value of  $Ri_B$  as a function of  $Re$  would be the line following the top of the steep slope

that bounds Regions I and III at the low  $Re$  limit, as illustrated by the bold dashed line in Figure 7, and represented approximately as

$$Ri_{Bc} = nRe^m \quad (21)$$

with  $n = 3.11 \times 10^{-6}$ , and  $m = 1.63$ . This line suggests a critical value of  $Ri_B$  on the order of 1 to 10 for laboratory scales and greater than 100 at geophysical scales. Note that this line does not extend to  $Ri_B$  values below the critical  $Ri$  value of  $\frac{1}{4}$  at  $Re = 1 \times 10^3$ . This position lies inside the upper limit of the gradient range,  $Re = 10^4$  ( $\frac{h}{L} \sim 100$ ), and thus represents a position in parameter space where turbulence initiation is controlled by the gradient, or  $Ri_g$ , value. However, based on this interpretation, it could be argued that the value of  $Re = 1 \times 10^3$  represents a more refined value of the upper limit of the gradient range.

While the bold dashed line in Figure 7, and the analogous equation in (Equation 21) represent a tempting relationship to define a critical value for  $Ri_B$ , it should be viewed with caution given that no data exists above this line, save for a few laboratory experiments from Yuan and Horner-Devine (2013) which lie within the gradient range. Thus, the steep slope forming the bounding feature identified by the bold dashed line is due only to the extrapolation of empirical representations of both the Likelihood and Energy Compression mechanisms. Further observational or numerical confirmation of this relationship would be beneficial.

## 5 Conclusions

The concept of the Richardson number as an indicator of turbulence in stratified flows has been a foundational concept in physical oceanography even prior to the groundbreaking work of Miles (1961) and Howard (1961) establishing  $\frac{1}{4}$  as a critical threshold for the value of  $Ri_g$ . As a “necessary but not sufficient” condition for the establishment of turbulence this metric has proven invaluable in the interpretation of numerous field, laboratory, and modelling results over the last six decades, and is a critical underpinning of turbulence closures (e.g., Burchard and Baumert, 1995). However, across sufficiently large scales (characterized by the bulk Richardson number), the concept of a critical Richardson number equal to  $\frac{1}{4}$  breaks down, as turbulence is routinely seen at  $Ri_B$  values significantly exceeding that critical value.

Here, we have proposed an appropriate range for the gradient Richardson number, consistent with  $10^2 \lesssim Re \lesssim 10^4$ , or  $10 \lesssim (\frac{h}{L}) \lesssim 100$ , based on turbulent spectral and energetics analyses. Building on the existence of this range, we hypothesize the importance of two proposed mechanisms, the first, referred to as the “likelihood mechanism”, provides a means for thicker stratified shear layers to sustain turbulence at  $Ri$  values exceeding the critical value of  $1/4$ , through the existence of smaller scale regions (on the order of the gradient range), where local values of  $Ri_g$  do fall below  $\frac{1}{4}$ . The second mechanism, referred to as the “energy compression mechanism”, explains why stronger turbulence is observed in thinner layers (i.e., values of  $CDi$  are up to 2 orders of magnitude higher at values of  $Re < 10^5$ , compared to  $Re > 10^5$ ) due to the low

energy threshold for excitation of turbulence in the unstratified regions above and below the shear-stratified layer. This results in the majority of turbulent energy doing useful work within the narrow confines of the layer and increasing the density of TKE in that region. Further analysis suggests that natural processes tend to push natural systems towards one of several “convergence zones” in the  $Ri - Re$  plane, while also suggesting a means to approximate a critical value for  $Ri_B$  at larger scales.

Overall, the results of this study may allow for a broader understanding of turbulence observations within  $Re-Ri$  parameter space, potentially yielding: (1) new insights into turbulence closures, particularly at lower  $Re$  values, which may yield more skillful modeling predictions across a range of scales. New closures may incorporate  $Re$  as a key factor in establishing mixing rates. While these changes are unlikely to affect mixing at full oceanographic scales, they may more adequately simulate mixing in environments with relatively thin shear stratified layers, or modeling of laboratory experiments designed to investigate ocean scale flows. (2) A more rigorous approach to defining critical values of  $Ri_B$ , which may greatly facilitate interpretation of observational data. The critical value of  $Ri_g < 1/4$  is often invoked in the interpretation of observational data at scales much larger than the gradient range. This study provides a better framework for using values of  $Ri$  in a prognostic or predictive capacity, and will aid in interpreting data from coarsely resolved density and shear profiles. (3) A more rigorous framework for the use of direct numerical simulation (DNS) results and laboratory experiments of turbulence to inform geophysical scale dynamics. DNS, in particular, has become a widespread and useful tool to better understand the energetics of turbulence at small scales in order to better understand ocean mixing. However, as discussed in detail above, the scales at which most DNS models can simulate turbulence are several orders of magnitude smaller than most oceanographic scales, and the mechanisms for scale, represented by  $Re$ , to impact mixing and turbulence presented in this study can provide an essential bridge for connecting DNS results to ocean-scale turbulence.

## Data availability statement

The original contributions presented in the study are included in the article/[Supplementary Material](#). Further inquiries can be directed to the corresponding author/s.

## Author contributions

DM: Formal analysis, Resources, Visualization, Writing - original draft, Project administration, Data curation, Writing - review & editing, Conceptualization, Funding acquisition, Investigation, Methodology. LG: Writing - original draft, Formal analysis, Methodology.

## Funding

The author(s) declared that financial support was received for this work and/or its publication. This work was funded by Office of Naval Research Physical Oceanography Program (N00014-15-1-2456, N00014-16-1-2441), and the National Science Foundation Physical Oceanography Program (OCE-1756599).

## In memoriam

This work is dedicated to the memory of co-author LG, who passed away in 2023, while this manuscript was in preparation. Lou's scientific passion was ocean turbulence, and he left his mark on the field in many ways. His energy and enthusiasm for life are sorely missed by all of us who were fortunate to know him and call ourselves friends and colleagues.

## Conflict of interest

The author(s) declared that this work was conducted in the absence of any commercial or financial relationships that could be construed as a potential conflict of interest.

## Generative AI statement

The author(s) declared that generative AI was not used in the creation of this manuscript.

Any alternative text (alt text) provided alongside figures in this article has been generated by Frontiers with the support of artificial intelligence and reasonable efforts have been made to ensure accuracy, including review by the authors wherever possible. If you identify any issues, please contact us.

## Publisher's note

All claims expressed in this article are solely those of the authors and do not necessarily represent those of their affiliated organizations, or those of the publisher, the editors and the reviewers. Any product that may be evaluated in this article, or claim that may be made by its manufacturer, is not guaranteed or endorsed by the publisher.

## Supplementary material

The Supplementary Material for this article can be found online at: <https://www.frontiersin.org/articles/10.3389/fmars.2026.1758561/full#supplementary-material>

## References

- Arneborg, L., Fiekas, V., Umlauf, L., and Burchard, H. (2007). Gravity current dynamics and entrainment—A process study based on observations in the Arkona Basin. *J. Phys. Oceanogr.* 37, 2094–2113. doi: 10.1175/JPO3110.1
- Avsarkisov, V. (2020). On the buoyancy subrange in stratified turbulence. *Atmosphere* 11, 659. doi: 10.3390/atmos11060659
- Balmforth, N. J., Llewellyn Smith, S. G., and Young, W. R. (1998). Dynamics of interfaces and layers in a stratified turbulent fluid. *J. Fluid Mech.* 355, 329–358. doi: 10.1017/S0022112097007970
- Baringer, M. O., and Price, J. F. (1997). Mixing and spreading of the Mediterranean outflow. *J. Phys. Oceanogr.* 27, 1654–1677. doi: 10.1175/1520-0485(1997)027<1654:MASOTM>2.0.CO;2
- Bartello, P., and Tobias, S. M. (2013). Sensitivity of stratified turbulence to the buoyancy Reynolds number. *J. Fluid Mechanics* 725, 1–22. doi: 10.1017/jfm.2013.170
- Buch, E. (1980). *On entrainment and vertical mixing in stably stratified fjords, Proceedings, 2nd International Symposium on Stratified Flows, Trondheim.* (Trondheim: Tapir).
- Burchard, H., and Baumert, H. (1995). On the performance of a mixed-layer model based on the k2e turbulence closure. *J. Geophysical Res.* 100, 8523–8540. doi: 10.1029/94JC03229
- Burchard, H., and Rippeth, T. P. (2009). Generation of bulk shear spikes in shallow stratified tidal seas. *J. Phys. Oceanogr.* 39, 969–985. doi: 10.1175/2008JPO4074.1
- Canuto, V. M., Cheng, Y., and Howard, A. M. (2010). An attempt to derive the  $\epsilon$  equation from a two-point closure. *J. Atmos. Sci.* 67, 1678–1685. doi: 10.1175/2009JAS3290.1
- Carr, J., Mariotti, G., Fahgerazzi, S., McGlathery, K., and Wiberg, P. (2018). Exploring the impacts of seagrass on coupled marsh-tidal flat morphodynamics. *Front. Environ. Sci.* 6. doi: 10.3389/fenvs.2018.00092
- Caulfield, C. P. (2020). Open questions in turbulent stratified mixing: do we even know what we do not know? *Phys. Rev. Fluids* 5, 110518. doi: 10.1103/PhysRevFluids.5.110518
- Caulfield, C. (2021). Layering, instabilities, and mixing in turbulent stratified flows. *Annu. Rev. Fluid Mech.* 53, 113–145. doi: 10.1146/annurev-fluid-042320-100458
- Cenedese, C., and Adduce, C. (2008). Mixing in a density-driven current flowing down a slope in a rotating fluid. *J. Fluid Mech.* 604, 369–388. doi: 10.1017/S0022112008001237
- Cenedese, C., and Adduce, C. (2010). A new parameterization for entrainment in overflows. *J. Phys. Oceanogr.* 40, 1835–1850. doi: 10.1175/2010JPO4374.1
- Chandrasekhar, S. (1961). *Hydrodynamic and Hydromagnetic Stability* (Oxford: Clarendon Press).
- Christodoulou, G. C. (1986). Interfacial mixing in stratified flows. *J. Hydraul. Res.* 24, 77–92. doi: 10.1080/00221688609499323
- Chu, V. H., and Vanvari, M. R. (1976). Experimental study of turbulent stratified shearing flow. *J. Hydraul. Div.* 102, 13598–1362. ASCE. doi: 10.1061/JYCEAJ.0004551
- Dallimore, C. J., Imberger, J., and Ishikawa, T. (2001). Entrainment and turbulence in saline underflow in Lake Ogawara. *J. Hydraul. Eng.* 127, 937–948. doi: 10.1061/(ASCE)0733-9429(2001)127:11(937)
- Delatolas, N., MacDonald, D. G., Goodman, L., Whitney, M. M., Huguenard, K., and Cole, K. L. (2023). Comparison of structure and turbulent mixing between lateral and leading-edge river plume fronts: Microstructure observations from a T-REMUS AUV. *Estuar. Coast. Shelf Sci.* 283, 108234. doi: 10.1016/j.ecss.2023.108234
- Drazin, P. G., and Reid, W. H. (1981). *Hydrodynamic Stability* (Cambridge, UK: Cambridge University Press).
- Ellison, T. H., and Turner, J. S. (1959). Turbulent entrainment in stratified flows. *J. Fluid Mechanics* 6, 423–448. doi: 10.1017/S0022112059000738
- Fer, I., Voet, G., Seim, K. S., Rudels, B., and Latarius, K. (2010). Intense mixing of the Faroe Bank Channel overflow. *Geophys. Res. Lett.* 37, L02604. doi: 10.1029/2009GL041924
- Ferron, B., Mercier, H., Speer, K., Gargett, A., and Polzin, K. (1998). Mixing in the romanche fracture zone. *J. Phys. Oceanogr.* 28, 1929–1945. doi: 10.1175/1520-0485(1998)028<1929:MITRFZ>2.0.CO;2
- Fong, D. A., and Geyer, W. R. (2001). Response of a river plume during an upwelling favorable wind event. *J. Geophys. Res.* 106, 1067–1084. doi: 10.1029/2000jc900134
- Forryan, A., Martin, A. P., Srokosz, M. A., Popova, E. E., Painter, S. C., and Renner, A. H. H. (2013). A new observationally motivated Richardson number based mixing parameterization for oceanic mesoscale flow. *J. Geophys. Res. Oceans* 118, 1405–1419. doi: 10.1002/jgrc.20108
- Girton, J. B., and Sanford, T. B. (2003). Descent and modification of the overflow plume in Denmark Strait. *J. Phys. Oceanogr.* 33, 1351–1364. doi: 10.1175/1520-0485(2003)033<1351:DAMOTO>2.0.CO;2
- Giunta, V., and Ward, B. (2022). Ocean mixed layer depth from dissipation. *J. Geophysical Res.: Oceans* 127, e2021JC017904. doi: 10.1029/2021JC017904
- Gregg, M. C. (1987). Diapycnal mixing in the thermocline: A review. *J. Geophys. Res.* 92, 5249–5286. doi: 10.1029/JC092iC05p05249
- Gregg, M., D'Asaro, E., Riley, J., and Kunze, E. (2018). Mixing efficiency in the ocean. *Annu. Rev. Mar. Sci.* 10, 443–473. doi: 10.1146/annurev-marine-121916-063643
- Holleman, R., Geyer, W., and Ralston, D. (2016). Stratified turbulence and mixing efficiency in a salt wedge estuary. *J. Phys. Oceanogr.* 46, 1769–1783. doi: 10.1175/JPO-D-15-0193.1
- Howard, L. (1961). Note on a paper of John W. Miles. *J. Fluid Mechanics* 10, 509–512. doi: 10.1017/S0022112061000317
- Howland, C. J., Taylor, J. R., and Caulfield, C. P. (2018). Testing linear marginal stability in stratified shear layers. *J. Fluid Mech.* 839, R4. doi: 10.1017/jfm.2018.79
- Imberger, J. (1994). “Transport processes in lakes: A review,” in *Limnology now: A paradigm of planetary problems*. Ed. R. Margalef (Amsterdam: Elsevier), 99–193.
- Ivey, G. N., and Imberger, J. (1991). On the nature of turbulence in a stratified fluid: I. The energetics of mixing. *J. Phys. Oceanogr.* 21, 650–658. doi: 10.1175/1520-0485(1991)021<0650:OTNOTI>2.0.CO;2
- Johnson, G. C., Lueck, R. G., and Sanford, T. B. (1994). Stress on the Mediterranean outflow plume. Part II: Turbulent dissipation and shear measurements. *J. Phys. Oceanogr.* 24, 2084–2092. doi: 10.1175/1520-0485(1994)024<2084:SOTMOP>2.0.CO;2
- Jurisa, J. T., Nash, J. D., Moum, J. N., and Kilcher, L. F. (2016). Controls on turbulent mixing in a strongly stratified and sheared tidal river plume. *J. Phys. Oceanogr.* 46, 2373–2388. doi: 10.1175/JPO-D-15-0156.1
- Kato, H., and Phillips, O. M. (1969). On the penetration of a turbulent layer into a stratified fluid. *J. Fluid Mechanics* 37, (4). doi: 10.1017/S0022112069000784
- Kilcher, L. F., Nash, J. D., and Moum, J. N. (2012). The role of turbulence stress divergence in decelerating a river plume. *J. Geophys. Res.* 117, C05032. doi: 10.1029/2011JC007398
- Kolmogorov, A. (1941). “The Local Structure of Turbulence in Incompressible Viscous Fluid for Very Large Reynolds' Numbers”, *Akademiia Nauk SSSR Doklady*, 30, 301–305.
- Lawrence, G. A., Tedford, E. W., and Carpenter, J. R. (2013). “Instabilities in stratified shear flow,” in *Coherent Flow Structures at Earth's Surface*. Eds. J. G. Venditti, J. L. Best, M. Church and R. J. Hardy. (Hoboken NJ: Wiley-Blackwell). doi: 10.1002/9781118527221.ch5
- Lozovatsky, I. D., and Fernando, H. J. S. (2013). Mixing efficiency in natural flows. *Phil. Trans. R. Soc. A* 371, 20120213. doi: 10.1098/rsta.2012.0213
- MacDonald, D. G., Carlson, J. O., and Goodman, L. (2013). On the heterogeneity of shear-stratified turbulence: Observations from a near-field river plume. *J. Geophys. Res. Oceans* 118, 6223–6237. doi: 10.1002/2013JC008891
- MacDonald, D. G., and Chen, F. (2012). Enhancement of turbulence through lateral spreading in a stratified-shear flow: Development and assessment of a conceptual model. *J. Geophys. Res.* 117, C05025. doi: 10.1029/2011JC007484
- MacDonald, D. G., and Geyer, W. R. (2004). Turbulent energy production and entrainment at a highly stratified estuarine front. *J. Geophys. Res.* 109, C05004. doi: 10.1029/2003JC002094
- MacDonald, D. G., Goodman, L., and Hetland, R. D. (2007). Turbulent dissipation in a near-field river plume: A comparison of control volume and microstructure observations with a numerical model. *J. Geophys. Res.* 112, C07026. doi: 10.1029/2006JC004075
- Mashayek, A., Caulfield, C. P., and Peltier, W. (2017). Role of overturns in optimal mixing in stratified mixing layers. *J. Fluid Mechanics* 826, 522–552. doi: 10.1017/jfm.2017.374
- Matsumoto, H., and Nakayama, K. (2024). Quantification of mixing depth using the gradient Richardson number in submerged aquatic vegetation meadows. *Water Resour. Res.* 60, e2023WR036472. doi: 10.1029/2023WR036472
- Mauritzen, C., Price, J. F., Sanford, T. B., and Torres, D. (2005). Circulation and mixing in the faroese channels. *Deep-Sea Res. I* 52, 883–913. doi: 10.1016/j.dsr.2004.11.018
- McCabe, R., Hickey, B. M., and MacCready, P. (2008). Observational estimates of entrainment and vertical salt flux in the interior of a spreading river plume. *J. Geophys. Res.* 113, C08027. doi: 10.1029/2007JC004361
- Miles, J. W. (1961). On the stability of heterogeneous shear flows. *J. Fluid Mech.* 10, 496–508. doi: 10.1017/S0022112061000305
- Nasmyth, P. W. (1970). *Ocean Turbulence. Ph.D. thesis* (British Columbia Canada: University of British Columbia).
- Nathaniel, J., Inall, M., Fraser, N., and Jones, S. (2024). “Dense water cascades in the rockall trough,” in *OCEANS 2024 - Halifax* (Halifax, NS, Canada: IEEE Xplore), 1–10. doi: 10.1109/OCEANS55160.2024.10754125

- Palma, V., MacDonald, D., and Raessi, M. (2024). The effect of domain length and initialization noise on direct numerical simulation of shear stratified turbulence. *Fluids* 9, 171. doi: 10.3390/fluids9080171
- Pedersen, F. B. (1980). *A monograph on turbulent entrainment and friction in a two-layer stratified flow*, Inst. Of Hydrodynamics and Hydraulic Eng. Techn. U. Denmark, Series Paper No. 25. (Denmark: DTU, Kongens Lyngist).
- Peltier, W. R., and Caulfield, C. P. (2003). Mixing Efficiency in Stratified Shear Flows. *Annu. Rev. Fluid Mech.* 35, 135–167. doi: 10.1146/annurev.fluid.35.101101.161144
- Peters, H., and Johns, W. E. (2005). Mixing and entrainment in the Red Sea outflow plume. Part II: Turbulence characteristics. *J. Phys. Oceanogr.* 35, 584–600. doi: 10.1175/JPO2689.1
- Piffer Braga, A., MacDonald, D. G., Delatolas, N., Goodman, L., Huguenard, K., Whitney, M. M., et al. (2025). Tracking and characterizing an evolving ocean feature: high-resolution sampling of a river plume front with an uncrewed underwater vehicle and aerial drone. *J. Atmospheric Oceanic Technol.* 42, 1469–1485. doi: 10.1175/JTECH-D-24-0121.1
- Pollard, R. T., Rhines, P. B., and Thompson, R. O. R. Y. (1973). The deepening of the wind-mixed layer. *Geophysical Fluid Dynamics* 3, 381–404. doi: 10.1080/03091927208236105
- Price, J. F. (1979). On the scaling of stress-driven entrainment experiments. *J. Fluid Mech.* 90, 509–529. doi: 10.1017/S0022112079002366
- Price, J. F., Weller, R. A., and Pinkel, R. (1986). Diurnal cycling: Observations and models of the upper ocean response to diurnal heating, cooling, and wind mixing. *J. Geophys. Res.* 91, 8411–8427.
- Riley, J. J., and de Bruyn Kops, S. M. (2003). Dynamics of turbulence strongly influenced by buoyancy. *Phys. Fluids* 15, 2047. doi: 10.1063/1.1578077
- Saggio, A., and Imberger, J. (2001). Mixing and turbulent fluxes in the metalimnion of a stratified lake. *Limnol. Oceanography* 46, 392–409. doi: 10.4319/lo.2001.46.2.0392
- Salehipour, H., Caulfield, C., and Peltier, W. (2016a). Turbulent mixing due to the Holmboe wave instability at high Reynolds number. *J. Fluid Mechanics* 803, 591–621. doi: 10.1017/jfm.2016.488
- Salehipour, H., and Peltier, W. (2019). Deep learning of mixing by two 'atoms' of stratified turbulence. *J. Fluid Mechanics* 861, R4. doi: 10.1017/jfm.2018.980
- Salehipour, H., Peltier, W., and Caulfield, C. (2018). Self-organized criticality of turbulence in strongly stratified mixing layers. *J. Fluid Mechanics* 856, 228–256. doi: 10.1017/jfm.2018.695
- Salehipour, H., Peltier, W. R., Whalen, C. B., and MacKinnon, J. A. (2016b). A new characterization of the turbulent diapycnal diffusivities of mass and momentum in the ocean. *Geophys. Res. Lett.* 43, 3370–3379. doi: 10.1002/2016GL068184
- Shih, L. H., Koseff, J. R., Ferziger, J. H., and Rehman, C. R. (2000). Scaling and parameterization of stratified homogeneous turbulent shear flow. *J. Fluid Mechanics* 412, 1–20. doi: 10.1017/S0022112000008405
- Smyth, W. D., and Moum, J. N. (2000). Length scales of turbulence in stably stratified mixing layers. *Phys. Fluids* 12, 1327–1342. doi: 10.1063/1.870385
- Smyth, W. D., and Moum, J. N. (2013). Marginal instability and deep cycle mixing in the eastern equatorial Pacific Ocean. *Geophys. Res. Lett.* 40, 1–5. doi: 10.1002/2013GL058403
- Smyth, W. D., Moum, J. N., and Caldwell, D. R. (2001). The efficiency of mixing in turbulent patches: Inferences from direct simulations and microstructure observations. *J. Phys. Oceanogr.* 31, 1969–1992. doi: 10.1175/1520-0485(2001)031<1969:TEOMIT>2.0.CO;2
- Smyth, W. D., Nash, J. D., and Moum, J. N. (2019). Self-organized criticality in geophysical turbulence. *Sci. Rep.* 9, 3747. doi: 10.1038/s41598-019-39869-w
- Smyth, W. D., and Peltier, W. R. (1989). The transition between kelvin-helmholtz and holmboe instability: an investigation of the over-reflection hypothesis. *J. Atmos. Sci.* 46, 3698–3720. doi: 10.1175/1520-0469(1989)046<3698:TTBKAH>2.0.CO;2
- Strang, E. J., and Fernando, H. J. S. (2001). Entrainment and mixing in stratified shear flows. *J. Fluid Mech.* 428, 349–386. doi: 10.1017/S0022112000002706
- Tennekes, H., and Lumley, J. L. (1972). *A first course in turbulence* (Cambridge, MA, USA: MIT press).
- Thorpe, S. A. (1969). Experiments on the stability of stratified shear flows. *Radio Sci.* 4, 1327–1331. doi: 10.1029/RS004i012p01327
- Thorpe, S., and Liu, Z. (2009). Marginal instability? *J. Phys. Oceanogr.* 39, 2373–2381. doi: 10.1175/2009JPO4153.1
- Umlauf, L., and Burchard, H. (2003). A generic length-scale equation for geophysical turbulence models. *J. Mar. Res.* 61, 235–265. doi: 10.1357/002224003322005087
- Venayagamoorthy, S. K., and Koseff, J. R. (2016). On the flux Richardson number in stably stratified turbulence. *J. Fluid Mech.* 798, R1. doi: 10.1017/jfm.2016.340
- Wells, M., Cenedese, C., and Caulfield, C. P. (2010). The relationship between flux coefficient and entrainment ratio in density currents. *J. Phys. Oceanogr.* 40, 2713–2727. doi: 10.1175/2010JPO4225.1
- Wijesekera, H. W., and Dillon, T. M. (1997). Shannon entropy as an indicator of age for turbulent overturns in the oceanic thermocline. *J. Geophys. Res.* 102, 3279–3291. doi: 10.1029/96JC03605
- Yuan, Y., and Horner-Devine, A. R. (2013). Laboratory investigation of the impact of lateral spreading on buoyancy flux in a river plume. *J. Phys. Oceanogr.* 43, 2588–2610. doi: 10.1175/JPO-D-12-0117.1
- Zhou, Z., Yu, X., Hsu, T.-J., Shi, F., Geyer, W. R., and Kirby, J. T. (2017). On hydrostatic coastal model simulations of shear instabilities in a stratified shear flow at high Reynolds number. *J. Geophys. Res. Oceans* 122, 3081–3105. doi: 10.1002/2016JC012334

## Appendix: Empirical parameter space mapping of $C_{Di}$

In the manuscript we explain that the value of  $C_{Di}$  is based on a general relationship between  $C_{Di}$  and  $Ri_B$ , modified by both the likelihood (Figure 5) and energy compression (Figure 6) mechanisms. An empirical function,  $\Phi_n$  is defined based on each proposed mechanism, such that  $C_{Di}$  can then be predicted as:

$$C_{Di} = C_{Dio} \Phi_B \Phi_L \Phi_C \quad (A1)$$

where  $\Phi_B$ ,  $\Phi_L$ , and  $\Phi_C$  represent functions associated with specific proposed mechanisms. Each empirical function is constrained by several coefficients, the values of which are determined by a global least squares fit to the available data. By using a mechanistically driven empirical approach, the functionality of  $C_{Di}$  can be explored, while developing a road map for more focused physical analysis of each relationship.

**Base Relationship:** The empirical function,  $\Phi_B$ , is designated to represent the observed trends in the base  $C_{Di}$  vs.  $Ri_B$  relationship:

$$\Phi_B = \left( 1 + \frac{1}{m_1 Ri_B^{n_1}} \right)^{-1} \quad (A2)$$

Here,  $m_1$ , which controls the  $Ri_B$  value associated with the roll off of  $C_{Di}$ , and  $n_1$ , which controls the slope of  $C_{Di}$  decay for low  $Ri_B$ , are coefficients for which best fit values are determined via the global least squares approach. An example of  $\Phi_B$  is shown in Figure 5a as the solid line.

**Likelihood Mechanism:** In order to capture this mechanism empirically, there are two dependencies to consider. First, the value of  $C_{Di}$  must roll off for increasing values of  $Ri_B$ . Second, the value of  $Ri_B$  which triggers the roll off must vary with  $Re$ , such that no roll off occurs at sufficiently high values of  $Re$ . To accomplish this, two empirical functions are used.  $\Phi_L$  describes the “likelihood” mechanism that controls the decay of  $C_{Di}$  as a function of  $Ri_B$ :

$$\Phi_L = \frac{1}{(1 + m_2 \Phi_{LS} Ri_B^{n_2})} \quad (A3)$$

Similar to (Equation A2), coefficients  $m_2$  and  $n_2$  control the rolloff location and slope, respectively. Note that  $m_2$  is modified by  $\Phi_{LS}$ , which defines the scale dependence of the “likelihood” mechanism by adjusting the rolloff location as a function of  $Re$ :

$$\Phi_{LS} = \frac{1}{(1 + m_3 (Re)^{n_3})} \quad (A4)$$

This function also exhibits a roll off and is equal to one for values of  $Re$  below a certain threshold. This functionality is essential to limit the decay in  $C_{Di}$  from occurring for cases where  $Ri_B$  is less than the critical value of  $Ri_g$ . Here,  $m_3$  and  $n_3$  similarly control rolloff location and slope. An example of  $\Phi_B \Phi_L$  is shown in Figure 5b as the dash-dot line.

**Energy Compression Mechanism:**  $\Phi_C$  is the empirical function used to capture the variability of this mechanism:

$$\Phi_C = 1 + \frac{1}{m_4 (Re)^{n_4}} \quad (A5)$$

where  $m_4$  and  $n_4$  similarly describe the upturn location and slope, respectively. An example of  $\Phi_C$  is superimposed as the solid line on the data in Figure 6. Again, the spread of the data is not intended to be wholly described by the solid line representing  $\Phi_C$ , as much of the variability is the result of the other mechanisms described above, as well as an artifact of the assumption of constant  $Re$  for certain legacy data sets.

**Least Squares Fit:** Combining the effects of the base relationship, the likelihood mechanism, and the energy compression mechanism following (Equation A1), the empirical functions presented above can be combined to produce a predictive relationship for  $C_{Di}$ . This expression leaves a total of nine unresolved coefficients ( $m_1 - m_4, n_1 - n_4$ , and  $C_{Dio}$ ), which are determined using a best fit approach with the existing data set. The outcome of this effort yielded the coefficients presented in Table A1, with an  $R^2$  value of 0.76, and the example surface shown in Figure 7. Despite the wide range of coefficient values, the range of the three key empirical functions ( $\Phi_B, \Phi_L, \Phi_C$ ) in (Equation A1) indicate comparable impacts on the value of  $C_{Di}$  across reasonable representative ranges of  $Ri_B$  and  $Re$ , as shown in Table A2.

TABLE A1 Coefficients for empirical functions derived from iterative least squares analysis.

Coefficient	Value	Description
$C_{Di}$	$1.55 \times 10^{-4}$	Base $C_{Di}$ value
$m_1$	$6.27 \times 10^0$	Rolloff control for $\Phi_B$
$m_2$	$2.76 \times 10^6$	Rolloff control for $\Phi_L$
$m_3$	$8.86 \times 10^{-14}$	Rolloff control for $\Phi_{LS}$
$m_4$	$8.35 \times 10^{-16}$	Rolloff control for $\Phi_C$
$n_1$	$1.51 \times 10^0$	Slope control for $\Phi_B$
$n_2$	$1.00 \times 10^0$	Slope control for $\Phi_L$
$n_3$	$4.20 \times 10^0$	Slope control for $\Phi_{LS}$
$n_4$	$2.84 \times 10^0$	Slope control for $\Phi_C$

TABLE A2 Range of empirical functions utilizing coefficients shown in Table A1 with representative ranges of  $Ri_B = [10^{-3} \ 10^3]$  and  $Re = [10^2 \ 10^9]$ .

Function	Range
$\Phi_B$	$2 \times 10^{-4} - 1 \times 10^0$
$\Phi_L$	$3.6 \times 10^{-10} - 1 \times 10^0$
$\Phi_C$	$1 \times 10^0 - 3 \times 10^9$